Direct numerical simulation of an impinging jet into parallel disks

Shin-ichi Satake

Department of Mechanical Systems Engineering, Toyama University Gofuku, Toyama city, Toyama, Japan, and

Tomoaki Kunugi

Department of Mechanical Engineering, Faculty of Engineering, Tokai University, Hiratsuka, Kanagawa, Japan

Introduction

Impinging jet flow by arrays of nozzles is a useful method to promote heat removal from gas turbines, to flatten temperature steel slabs and dry paper and films. According to Martin (1977), there are two patterns in impinging flows. The first is a pattern in which a nozzle extrudes into space or a free jet impinges on a plate, such as Gardon and Akfirat (1966) employed. The second pattern is that of impinging flow into parallel disks. As mentioned above, many experimental studies have been carried out during the past three decades. On the other hand, several numerical studies regarding an impinging round jet flow have been carried out; Amano (1983) and Kunugi and Kawamura (1988) used a two-equation model of turbulence. These numerical results predicted the first peak of the local heat transfer near the stagnation point and were in very good agreement with the experimental data. Recently, Kunugi *et al.* (1993) and Craft *et al.* (1993), who used various Reynolds stress models of turbulence, predicted a "secondary peak" of the local heat transfer on the jet impingement plate. According to the experimental consideration by Gardon and Akfirat (1966), the reasons for the peak generation are seen that the first peak in the range of $0 < R/D < 0.5$ is caused by the flow acceleration and the secondary one in the range of $R/D > 0.5$ is caused by the flow transition from laminar to turbulent. Moreover, flow visualization photographs obtained by Yokobori *et al.* (1979) showed the toroidal vortices being convected on the impingement plane. From these experimental evidences, the mechanism of the flow transition near the first and secondary peak points can be explained by a first transition from turbulent to laminar at the first peak point and then the second transition from laminar to turbulent at the second peak point. In this sense, it is seen that the

flow-transition behavior can be affected by some vortex motion coming from the nozzle edge. However, no numerical study regarding both transition mechanisms has been reported. Therefore, a direct numerical simulation (DNS) will be very helpful to understand the entire flow feature of the impinging round jet.

The objectives of this study are to elucidate the flow mechanism by which eddies are generated at the edge of the nozzle and transported into the impingement region, and to understand the relationship between turbulence generation and vortex structures in the transition region.

Numerical procedure

The DNS code with cylindrical coordinates can numerically solve the momentum and continuity equations. A second-order finite volume discretization scheme is applied to the spatial derivatives on a staggered mesh system. In order to avoid a singularity at the center axis of the pipe center, the incompressible Navier-Stokes equation can be rewritten with a radial flux formulation, $q_r = r \times u_r$, $q_z = u_z$, $q_\theta = u_\theta$. In terms of q_r, the radial momentum equation in conservative form becomes

$$\frac{\partial q_r}{\partial t} + \frac{\partial q_z q_r}{\partial z} + \frac{\partial}{\partial r}\left(\frac{q_r^2}{r}\right) + \frac{1}{r}\frac{\partial q_\theta q_r}{\partial \theta} - q_\theta^2 = -r\frac{\partial p}{\partial r}$$
$$+ \frac{1}{Re_r}\left[\frac{\partial^2 q_r}{\partial z^2} + r\frac{\partial}{\partial r}\left(\frac{1}{r}\frac{\partial q_r}{\partial r}\right) + \frac{1}{r^2}\frac{\partial^2 q_r}{\partial \theta^2}\right] + \frac{1}{Re_r}\left[-\frac{2}{r}\frac{\partial q_\theta}{\partial \theta}\right] \qquad (1)$$

The above equation can be discretized as the same manner as Verzicco and Orlandi (1996). Control-volume location in the central region on the staggered grid system is defined as shown in Figure 1.

For example, the discretization form of the convective term for the radial component in equation (1) by using $q_{r,2}$, $q_{r,1}$, $q_{r,0}$ (in Figure 1) becomes
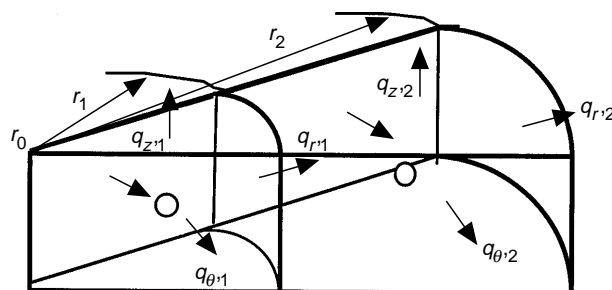
$$\iiint \frac{1}{\Delta r}\left(\frac{1}{r_{m2}}\left\{\frac{q_{r,2}+q_{r,1}}{2}\right\}^2 - \frac{1}{r_{m1}}\left\{\frac{q_{r,1}+q_{r,0}}{2}\right\}^2\right)r\Delta r\Delta\theta\Delta Z,$$ (2)

$$r_{m2} = (r_1 + r_2)/2, \; r_{m1} = (r_1 + r_0)/2$$

where the $q_{r,0}$, $q_{r,1}$ and $q_{r,2}$ are evaluated at grid points r_0, r_1 and r_2 respectively.

q_r is evaluated at the grid point $r = 0$, and there is zero. Thus the above equation is rewritten as

$$\iiint \frac{1}{\Delta r}\left(\frac{1}{r_{m2}}\left\{\frac{q_{r,2}+q_{r,1}}{2}\right\}^2 - \frac{1}{r_{m1}}\left\{\frac{q_{r,1}}{2}\right\}^2\right)r\Delta r\Delta\theta\Delta Z.$$ (3)

The discretization form of the viscous term for the radial component in the equation also may be expressed as

$$\iiint \frac{r_1}{\Delta r}\left(\frac{1}{r_{m2}}\left\{\frac{q_{r,2}-q_{r,1}}{\Delta r}\right\} - \frac{1}{r_{m1}}\left\{\frac{q_{r,1}-q_{r,0}}{\Delta r}\right\}\right)r\Delta r\Delta\theta\Delta Z,$$ (4)

giving the form below owing to substituting $q_{r,0} = 0$, in the above equation:

$$\iiint \frac{r_1}{\Delta r}\left(\frac{1}{r_{m2}}\left\{\frac{q_{r,2}-q_{r,1}}{\Delta r}\right\} - \frac{1}{r_{m1}}\left\{\frac{q_{r,1}}{\Delta r}\right\}\right)r\Delta r\Delta\theta\Delta Z.$$ (5)

Thus, q_r at the center will never be used from the above expression (see equations (3) and (5)).

The incompressible Navier-Stokes and continuity equations described in cylindrical coordinate are integrated in time using the fractional-step method by Dukowicz and Dvinsky (1992). The temporal discretization of the Navier-Stokes and continuity equations can be expressed as vector equations:

$$\frac{\partial q}{\partial t} = L(q) - N(q) - \nabla p$$ (6)

$$\nabla \cdot q = 0$$ (7)

where $L(q)$ is the linear term, $N(q)$ is the non-linear term, ∇ is the divergence operator, q is the velocity vector and ∇p is the pressure gradient term. A modified third-order Runge-Kutta scheme (Spalart *et al.*, 1991) is applied to the terms treated explicitly and the second-order Crank-Nicholson scheme is used for other terms implicitly. By using the intermediate velocity field q^k, equations (4) and (5) can be written in the following system of equations:

$$\nabla \cdot q^k = 0,$$ (8)

$$\frac{q^k - q^{k-1}}{\Delta t} = \beta_k \left(L(q^k) + L(q^{k-1}) \right) - \gamma_k N(q^{k-1}) - \zeta_k N(q^{k-2}) - 2\beta_k \nabla p \quad (9)$$

Superscript k ($k =1,2,3$) represents the Runge-Kutta sub-steps such that $q^k = q^n$ for $k =1$ and $q^k = q^{n+1}$ for $k =3$. Superscript n represents the full time-step. The coefficients, β_k, γ_k, ζ_k, are selected such that the total time advancement is third order accurate for the explicitly treated terms and second order accurate for implicitly treated terms (Spalart *et al.*, 1991). These coefficients are:

$$\beta_1 = 4/15, \ \beta_2 = 1/15, \ \beta_3 = 1/6, \gamma_1 = 8/15,$$

$$\gamma_2 = 5/15, \ \gamma_3 = 3/4, \zeta_1 = 0, \ \zeta_2 = -17/60, \ .$$

$$\zeta_3 = -5/12$$

The intermediate velocity field q^k must be globally divergence-free. The continuity equation is then corrected on each cell by the pressure increment $\delta p^k = p^k - p^{k-1}$:

$$q^k = q^{k-1} - 2\beta_k \Delta t \nabla \delta p^k . \quad (10)$$

Then, we have to solve the following Poisson equation:

$$\nabla^2 \delta p^k = \frac{1}{2\beta_k \Delta t} \nabla \cdot q^k \quad (11)$$

This expression is the so-called "delta-form". The above Poisson equation for $\delta \hat{p}^k$ can be solved by means of a combination of a Fourier transform method and ILUCGS method (Sonneveld, 1989). Since a uniform computational grid and a periodic boundary condition are used in the circumferential direction, the Fourier transform can be applied to the reduction of the three-dimensional Poisson equation (11) to a set of uncoupled two-dimensional equations:

$$\frac{1}{r}\frac{\partial}{\partial r}\left(r\frac{\partial \delta \tilde{p}^k}{\partial r} \right) + \frac{\partial^2 \delta \tilde{p}^k}{\partial z^2} - k'^2_\theta \cdot \delta \tilde{p}^k = \frac{1}{2\beta_k \Delta t} \nabla \cdot \hat{q}^k ,$$

$$k'^2_\theta = \frac{2}{r^2 \Delta \theta^2}\left[1 - \cos\left(\frac{2\pi m}{M_\theta} \right) \right], \ m = 0, \ M_\theta - 1 \quad (12)$$

where m is the wave number, M_θ is the number of cell and $r\Delta\theta$ is the grid spacing in the circumferencial direction. Equation (12) represents a banded, penta-diagonal matrix. In the calculation for this matrix, the ILUCGS method (Sonneveld, 1989) was employed for every wave number. This algorithm allows the use of a fast Fourier transform and thus substantially reduces the solution time. A message-passing system with eight nodes on a Fujitsu VPP500 vector-parallel supercomputer was used in this computation. Efficiency of

computation can be further enhanced by implementing the Fourier-ILUCGS method in parallel by computing a group of Fourier modes on a different processor.

Computational condition
Computational condition for fully developed turbulent pipe flow
In the first test case, we consider fully developed turbulent pipe flow and compare with previous DNS results (Akselvoll and Moin, 1995; Eggels, 1994) obtained for the same flow condition. The Reynolds number was 180 based on pipe radius and friction velocity. The objective of this simulations is to validate the numerical method developed for the impinging round jet. The computational domain of the fully developed turbulent pipe flow is exactly the same size as Eggels's DNS (Eggels, 1994) shown in Figure 2. The number of grid points is in the *z*-, *r*- and *θ*-directions respectively.

Computational condition for the turbulent impinging round jet
A computational domain of the turbulent impinging round jet confined with the parallel walls is exactly the same size as Nishino's experiment (Nishino *et al.*, 1996) shown in Figure 3. The experimental data provides a base for comparison with the computational results. The Reynolds number, which is based on the
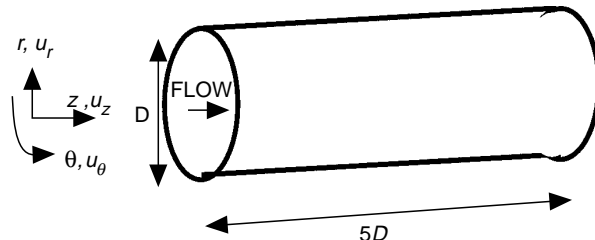
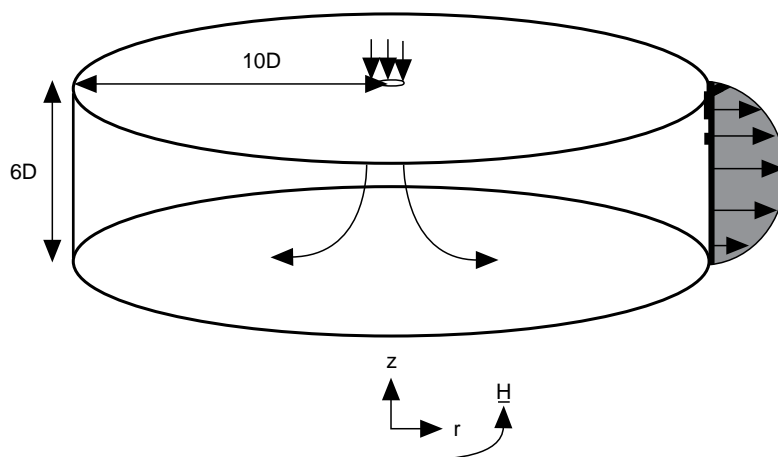

Figure 2.
Computational domain for turbulent pipe flow

Figure 3.
Computational domain for impinging jet with confined wall

nozzle exit velocity U_0 and the nozzle diameter (D), is assumed to be 10,000. Uniform mesh spacing is applied in the circumferential direction (θ). In the z-direction (z) and radial direction (r), non-uniform meshes specified by a hyperbolic tangent function are employed. The number of grid points is $192 \times 220 \times 192$ in the z-, r- and θ-directions respectively. The inlet boundary condition is connected with an "inflow generator," that is, the inlet turbulent pipe flow is considered. The number of computational grids for the "inflow generator" is $16 \times 41 \times 192$ points in the z-direction, radial and circumferential directions respectively. A convective boundary condition (Lowery *et al.*, 1987) is imposed at the exit of the computational domain. Note that the mass balance between the inflow and outflow must be maintained at every time step. The initial velocity field was generated from uniform velocity with random noise. The governing equations were integrated forward in time until the numerical solutions reached a statistical steady state. The computation was continued for about $3D/U_0$ in order to calculate the statistics for the ensemble averages of turbulent quantities over space and time. All the results discussed in the following section are based on non-dimensional parameters normalized by the nozzle exit velocity U_0 and the nozzle diameter D.

Results and discussion
Solution of the fully developed turbulent pipe flow
Several mean flow in pipe flow properties from the present DNS and reference DNS are listed in Table I. Uc is the center line velocity, C_f the friction coefficient, and Re_b is the Reynolds number based on the bulk velocity and pipe diameter. From Table I it appears that the present DNS results agree with previous DNS results.

The mean velocity profile normalized by the friction velocity is shown in Figure 4. There is good agreement with the DNS results of Eggels (1994) and Akselvoll and Moin (1995).

The turbulent intensities are shown in Figure 5. Minor deviations for the streamwise component are observed between the present DNS and Akselvoll and Moin's DNS. In the other components, excellent agreement is observed between the present DNS and previous DNS.

The budget of turbulent kinetic energy, normalized by the friction velocity, is shown in Figure 6 where a negligible residual error is evident. Note that the residual of the turbulent kinetic energy equation has to be zero.

Case	Re_b	U_c	U_b	U_c/U_b	C_f
Present	5,310	19.39	14.75	1.31	9.19×10^{-3}
Eggels *et al.* (1994)	5,303	19.31	14.73	1.31	9.22×10^{-3}
Akselvoll and Moin (1995)	5,292	19.32	14.70	1.31	9.25×10^{-3}

Table I.

Figure 4.
Comparison of mean
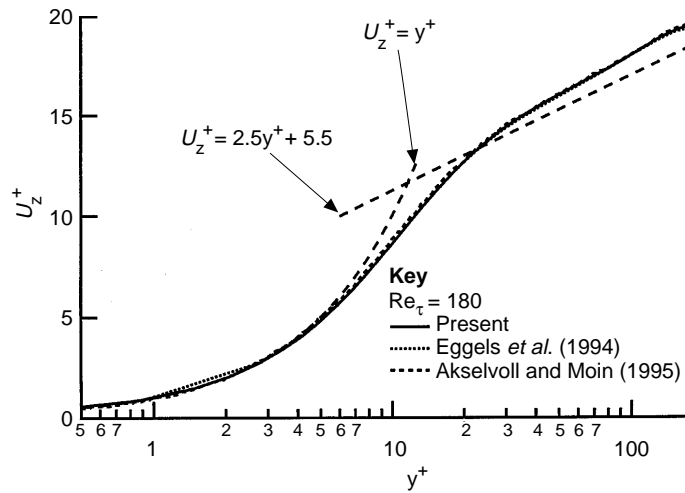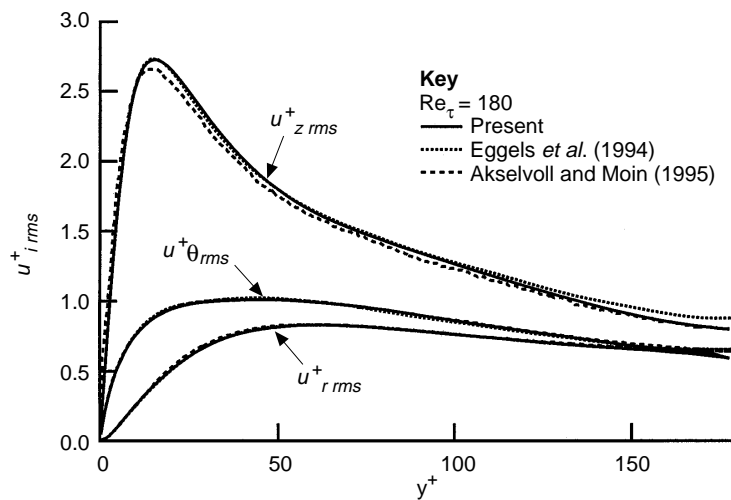axial velocity in
turbulent pipe flow

Figure 5.
Comparison of
turbulent intensities in
turbulent pipe flow

Solution of the impinging jet

Figure 7 presents the comparison between the DNS results and Nishino's experimental data (Nishino *et al.*, 1996) for the mean axial velocity profiles. The comparison is made at five representative locations; $r/D = 0.25$ at the inner nozzle, $r/D = 0.5$ at the nozzle edge, and three wall jet regions, $r/D = 1.0$, 1.95, 2.41. Excellent agreement between computational and experimental results is obtained in the wall jet region. At other stations, the present results are relatively larger than the experimental results. This is because the inlet boundary condition is different from the experimental condition, since a bell-mouth shape contraction was used as the inlet nozzle in the experiment. The
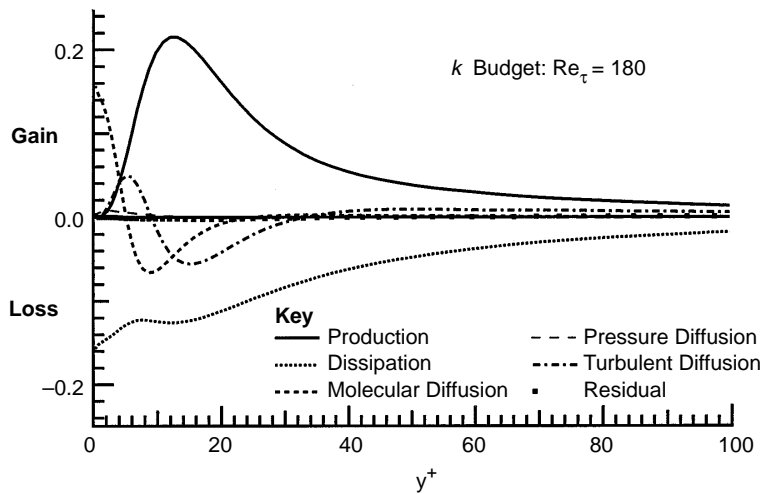
Simulation of an
impinging jet into
parallel disks

775

Figure 6.
The budget of turbulent
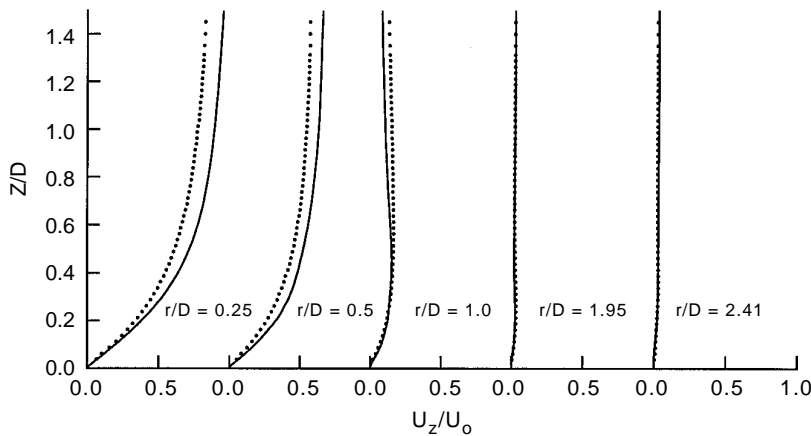kinetic energy in
turbulent pipe flow

Figure 7.
Comparison of mean
axial velocity profiles:
lines, present; symbols,
experimental data by
Nishino *et al.* (1996)

mean radial velocity profiles U_r/U_0 are shown in Figure 8. The peak velocity at the boundary layer is larger than that of the experiment, although the entire profiles at each radial location are in fairly good agreement with the experimental data.

Reynolds shear stress $-\overline{u_r' u_z'}$ distributions along the *z*-direction are shown in Figure 9. In the vicinity of the wall, negative values can be seen. Although the experimental data show more complicated distributions in the same region, the locations of negative $-\overline{u_r' u_z'}$ in both results are almost the same. The r.m.s. profiles of axial and radial velocity fluctuations are compared with the experimental data at five locations in Figures 10 and 11. In Figures 10 and 11, the values of $(\overline{u_z' u_z'})$ and $(\overline{u_r' u_r'})^{1/2}$ in the jet impingement region are relatively smaller than the experimental data because the present sampling time for statistical treatment is very small compared with the experiment. However, it is

Figure 8.
Comparison of mean
radial velocity profiles:
lines, present; symbols,
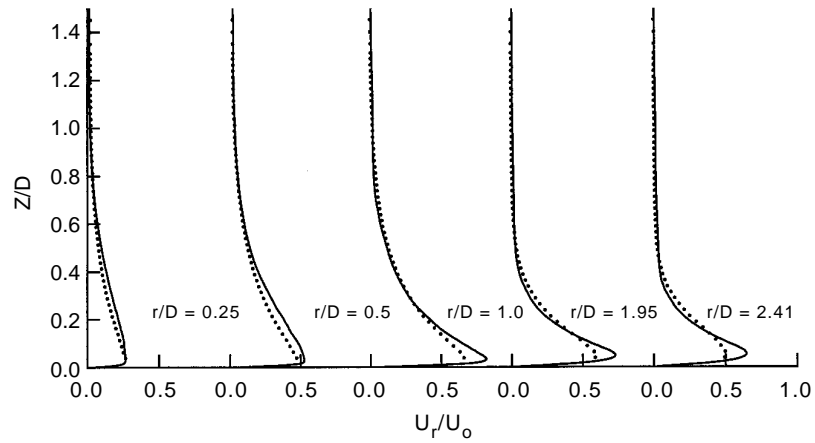experimental data by
Nishino *et al.* (1996)

Figure 9.
Comparison of Reynolds
stress profiles $-u_r'u_z'$:
lines, present; symbols,
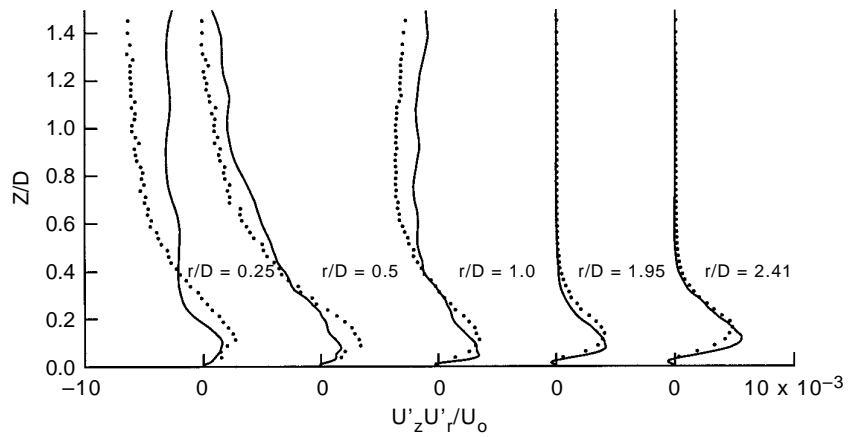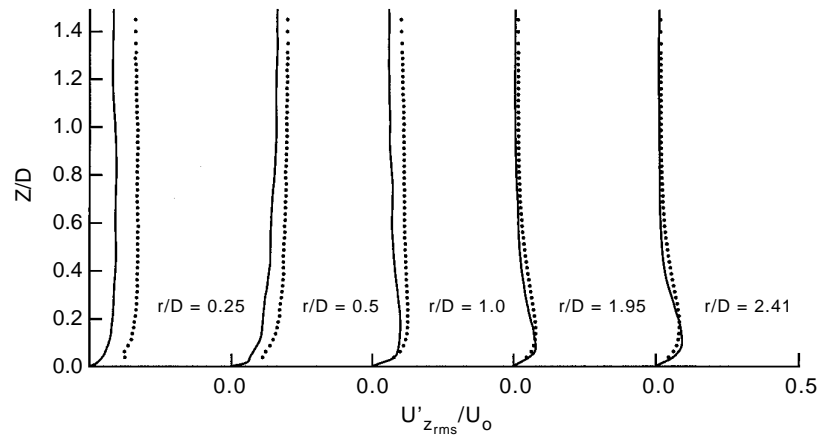experimental data by
Nishino *et al.* (1996)

Figure 10.
Comparison of Reynolds
stress profiles $(\overline{u_z'u_z'})^{1/2}$:
lines, present; symbols,
experimental data by
Nishino *et al.* (1996)

found that these profiles in the downstream region are in good agreement with the experimental data. Reynolds stress $(\overline{u_\theta' u_\theta'})^{1/2}$ profiles along the z-direction are shown in Figure 12. The profiles are similar to that of $(\overline{u_r' u_r'})^{1/2}$. Nishino *et al.* (1996) also observed the same behavior.

The budget of turbulent kinetic energy can be obtained by

$$P_k + \varepsilon_k + PD_k + C_k + TD_k + VD_k = 0 \qquad (13)$$

where: production is

$$P_k = -\overline{u_r'^2}\frac{\partial U_r}{\partial r} - \overline{u_r' u_z'}\frac{\partial U_r}{\partial z} - \overline{u_r' u_z'}\frac{\partial U_z}{\partial r} - \overline{u_z'^2}\frac{\partial U_z}{\partial z} - \overline{u_\theta'^2}\frac{U_r}{r}$$
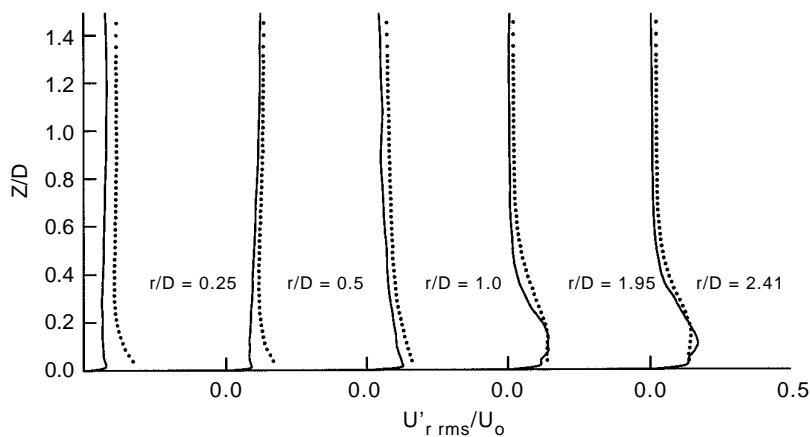
dissipation is

Figure 11.
Comparison of Reynolds stress profiles $(\overline{u_r' u_r'})^{1/2}$: lines, present; symbols, experimental data by Nishino *et al.* (1996)
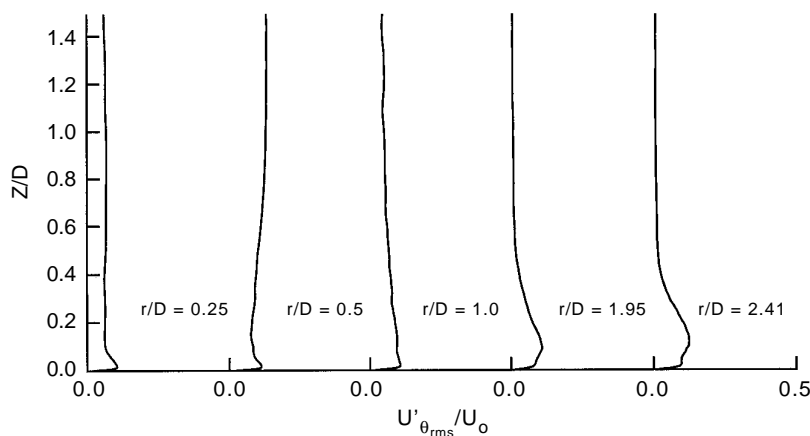

Figure 12.
Comparison of Reynolds stress profiles $(\overline{u_\theta' u_\theta'})^{1/2}$: lines, present; symbols, experimental data by Nishino *et al.* (1996)

$$\varepsilon_k = -\frac{1}{Re}\overline{\frac{\partial u_i}{\partial x_j}\frac{\partial u_i}{\partial x_j}}$$

pressure diffusion:

$$PD_k = -\left(\frac{\partial \overline{pu_r}}{\partial r} + \frac{\overline{pu_r}}{r} + \frac{\partial \overline{pu_z}}{\partial z}\right)$$

convection:

$$C_k = -U_r\frac{\partial k}{\partial r} - U_z\frac{\partial k}{\partial z}$$

turbulent diffusion:

$$TD_k = -\left(\frac{\partial \overline{u_r k}}{\partial r} + \frac{\overline{u_r k}}{r} + \frac{\partial \overline{u_z k}}{\partial z}\right)$$

viscous diffusion:

$$VD_k = \frac{1}{Re}\left(\frac{\partial^2 k}{\partial^2 r} + \frac{1}{r}\frac{\partial k}{\partial r} + \frac{\partial^2 k}{\partial z^2}\right)$$

The budgets of turbulent kinetic energy compared with Nishino's experimental data at $r/D = 0.5$ are shown in Figures 13 and 14. Some fluctuations of the curves obtained by the DNS are observed in all budget terms, but are most pronounced in the turbulent diffusion term. Although the sampling times are insufficient, the overall profiles of all terms are not very different from the

Figure 13.
Comparison of production and dissipation plus pressure diffusion terms in turbulent kinetic energy budget at $r/D = 0.5$: lines, present; symbols, experimental data by Nishono *et al.* (1996)
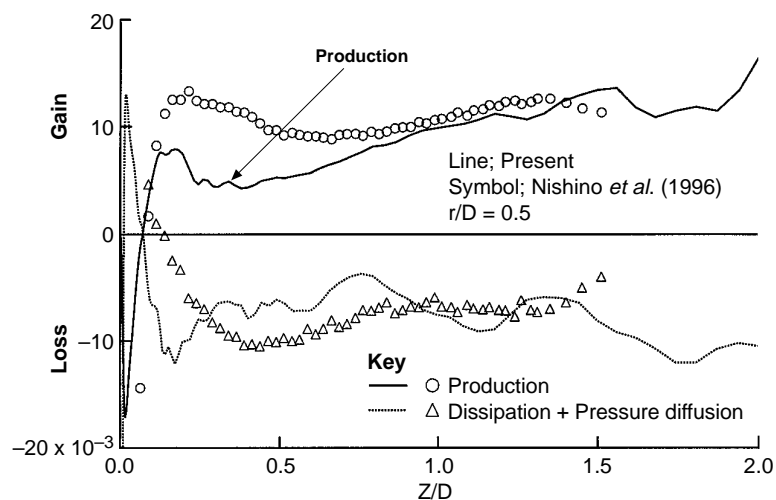
experimental data. The negative production in the present calculation is also observed in Figure 13. Figure 15 shows the three-dimensional contour surface of the low pressure region; $p'<-0.02$. The generation of vortex-rings below the nozzle edge and the vortex breaking about half way between the nozzle and the wall can be observed. In the impingement region, the vortex-ring column disappears and another big torus-shaped low pressure region forms in the downstream region. From the numerical visualization, it is found that the wall-layer streaks are elongated in the radial direction in the jet impingement region. The vortex generation and breaking processes and the generation and
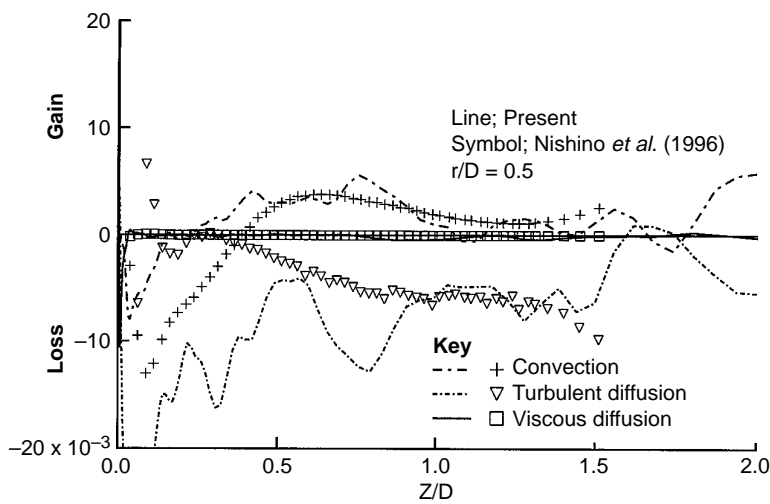
Figure 14.
Comparison of convection, turbulent diffusion and viscous diffusion terms in turbulent kinetic energy budget at $r/D = 0.5$: lines, present; symbols, experimental data by Nishono *et al.* (1996)
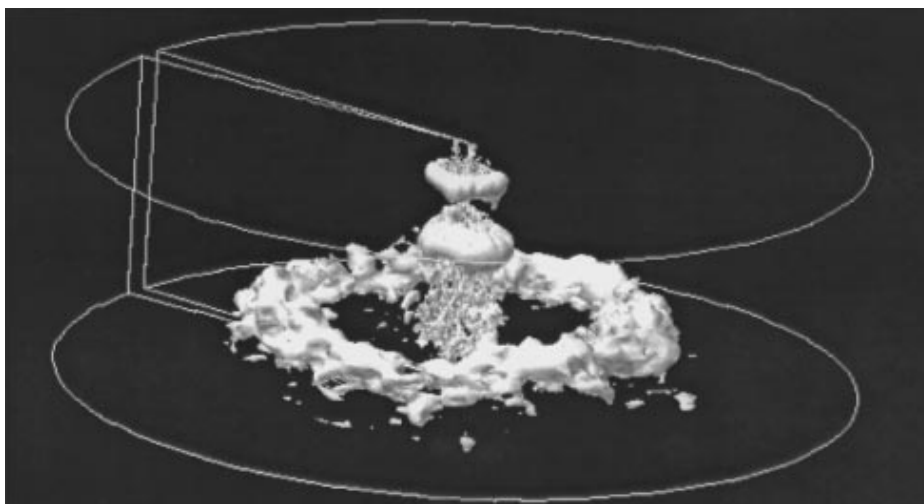

Figure 15.
3D contour surface of low pressure regions: White: $p'<-0.02$

elongation processes of the wall-streaks will be considered as the main mechanism of turbulence transition in this flow. Further investigation will be necessary to understand the entire turbulence transition processes for this kind of complex flow.

Summary

DNS on a turbulent impinging round jet was carried out for a Reynolds number of 10,000. The present results in the downstream region are in fairly good agreement with Nishino's experimental data. From the numerical visualization results in the jet impingement region, it is found that the wall-layer streaks are elongated in the radial direction.

References

Akselvoll, K. and Moin, P. (1995), "Large eddy simulation of turbulent confined coannular jets and turbulent flow over a backward facing step", Stanford University, TF-63.

Amano, R. (1983), "Turbulent effect on the impinging jet on a flat plate", *Bull. JSME,* Vol. 26 No. 221, pp. 1891-7.

Craft, T.J., Graham, L.J. and Launder, B.E. (1993), "Impinging jet studies for turbulence model assessment-II. An examination of the performance of four turbulence model", *Int. J. Heat Mass Transfer,* Vol. 36 No. 10, pp. 2685-93.

Dukowicz, J.K. and Dvinsky, A.S. (1992), "Approximate factorization as a high order splitting for the implicit incompressible flow equations," *Journal of Computerised Physics*, Vol. 102 No. 2, Academic Press Inc., USA, pp. 336-47.

Eggels, J.G.M. (1994), "Direct and large eddy simulation of turbulent flow in a cylindrical pipe geometry", PHD thesis, Delft University of Technology, The Netherlands.

Gardon, R. and Akfirat, J.C. (1966), "Heat transfer characteristics of imping two-dimensional air jets", *ASME Journal of Heat Transfer*, Vol. 88, pp. 101-8 .

Kunugi, T. and Kawamura, H. (1988), "Application of a two-equation turbulence model to heat transfer and fluid of an impinging round jet", *Transport Phenomena in Turbulent Flows,* Hemisphere, pp. 593-604.

Kunugi. T., Yokomine, T. and Ichimiya, K. (1993), "Numerical and experimental study on heat transfer of an impinging turbulent plane jet with confined wall", *ASME HTD*, Vol. 246, pp. 25-31.

Lowery, P.S., Reynolds, W.C. and Mansour, N.N. (1987), "Passive scalar entrainment and mixing in a forced spatially-developing mixing layer", AIAA paper 87-0142.

Martin, H. (1977), "Heat and mass transfer impinging gas jet and solid surface", *Advanced Heat Transfer,* Vol. 13, pp. 1-60 .

Nishino, K., Samada, M., Kasuya, K. and Torii, K.(1996), "Turbulence statics in the stagnation region of an axisymmetric impinging jet flow", *International Journal of Heat and Fluid Flow*, Vol. 17, pp. 193-201.

Sonneveld, P. (1989), "CGS: A first Lanczos-type solver for nonsymmetric linear systems", *SIAM Journal Sci. Statist. Compt.,* Vol. 10, pp. 36-52.

Spalart, P.R., Moser, R.D. and Rogers, M.M. (1991), "Spectral methods for the Navier-Stokes equations with one infinite and two periodic directions", *J. Comp. Phys.,* Vol. 96, pp. 297-324.

Verzicco, R. and Orlandi, P. (1996), "A finite-difference scheme for three-dimensional incompressible flows in cylindrical coordinate", *J. Comp.,Phys.,* Vol. 123, pp. 402-14.

Yokobori, S., Kasagi, N., Hirata, M., Nakamaru, M. and Haramura, Y. (1979), "Characteristics behavior of turbulence and transport phenomena at the stagnation region of an axi-symmetrical impinging jet", *Proc. 2nd Symp. Turb. Shear Flows*, London, UK, pp. 4.12-.17.